

Structural and Magnetic Reconstruction of Thermodynamically Stable CaMnO_3 (001) Surfaces

Diomedes Saldana-Greco, Chan-Woo Lee, Doyle Yuan, and Andrew M. Rappe

*The Makineni Theoretical Laboratories,
Department of Chemistry,
University of Pennsylvania,
Philadelphia, PA 19104-6323, USA*

(Dated: April 22, 2015)

Abstract

The relative thermodynamic stability of surface reconstructions including vacancies, adatoms and additional layers on both CaO and MnO_2 terminations is calculated to predict the surface phase diagram of $(\sqrt{2} \times \sqrt{2})R45^\circ$ CaMnO_3 (001) using *ab initio* thermodynamics. Stoichiometric and nonstoichiometric reconstructions are considered. A set of boundary conditions driven by the binary and ternary sub-phases from CaMnO_3 defines its bulk stability region, enclosing the stable surface reconstructions that can be in equilibrium with the bulk. Most of the surfaces take the magnetic ordering of the bulk ground state, G-type antiferromagnetic (AFM); however, some of the MnO_2 -terminated surfaces are more stable when the surface layer spins flip. At 573 K, the stoichiometric CaO - and MnO_2 -terminated surfaces are predicted to be thermodynamically stable, as well as a CaO -terminated surface reconstruction where half the Ca are replaced by Mn. The MnO_2 -terminated surface reconstructions dominate the phase diagrams at high temperatures, including phases with MnO and MnO_2 adatoms per surface unit cell.

I. INTRODUCTION

Perovskite CaMnO_3 has recently been the subject of increasing interest due to its strain-assisted multiferroicity [1, 2], thermoelectric efficiency [3, 4], colossal magnetoresistance [5], and catalytic properties [6]. Its high catalytic activity for oxidation reactions and structural similarity to important biological catalysts has motivated studies on CaMnO_3 as a potential catalyst for water oxidation [7]. While atomic insight into the CaMnO_3 surface is imperative if its potential application as a catalyst is to be realized, very little has been investigated in this direction. Most of the previous studies have focused on magnetic properties [8–10] of the stoichiometric cubic CaMnO_3 surface.

In this study, we determine the atomic and magnetic low-energy surface structures of orthorhombic $Pnma$ CaMnO_3 (001) as functions of environmental variables, developing surface phase diagrams by combining density functional theory (DFT) and thermodynamics [11]. Various surface reconstructions for both CaO - and MnO_2 -terminated surfaces are explored within a $(\sqrt{2} \times \sqrt{2})R45^\circ$ surface periodicity. For structures with Mn atoms at the surface, we considered multiple magnetic spin configurations to ensure that the surface stability accounts for the potential magnetic reconstruction at the surface. The surface free energies are computed to generate the surface phase diagram within the bulk stability range. To illustrate the surface stability at a range of temperatures, the vibrational free energy is included in the calculation of the bulk stability region. Through our surface examination, we predict thermodynamically stable surface reconstructions at a range of conditions.

II. METHODOLOGY

A. Computational Methods

DFT calculations were performed using the PBEsol [12] generalized gradient approximation (GGA), as implemented in the QUANTUM ESPRESSO [13] computer code. Perdew and collaborators have shown that the PBEsol functional describes solids and surfaces accurately [12]. PBEsol+ U was also used to test electronic properties, with $U_{\text{eff}} = 7.23$ eV, in line with previous work [14] and determined with the linear response scheme [15]. However, adding strong correlations to CaMnO_3 provides unsatisfactory description of the magnetic properties, as has been established by Luo *et al.* [14]. Spin-polarized electronic densities

were used in all calculations, treating the magnetic moments as collinear in all cases, with additional non-collinear (NC) calculations for some Mn-terminated surfaces and for the ternary sub-phases. All atoms are represented by norm-conserving, optimized [16], designed nonlocal [17] pseudopotentials with spin-orbit interaction (for NC magnetism). The pseudopotentials are generated with the OPIUM package [18], treating the $3s$, $3p$, $3d$, $4s$, and $4p$ of Ca, the $3s$, $3p$, $3d$, $4s$, and $4p$ of Mn, and the $2s$ and $2p$ of O as valence states. An accurate description of the magnetic properties of all the systems studied is achieved when nonlinear core-valence interaction is included in the Mn pseudopotential by the partial core correction scheme [19, 20]. The CaMnO_3 magnetic ground state is collinear G-type antiferromagnetic (AFM) with an observed Néel temperature of about 130 K [21], estimating the magnetic interaction energy to be around 6.6 meV [22]. Therefore, all calculations are run with a 70 Ry plane-wave energy cutoff to ensure accuracy for the small relative energies among the different magnetic configurations. The Brillouin zone is sampled using a $4 \times 4 \times 1$ Monkhorst-Pack [23] k -point mesh for surface structures based on energy convergence for bulk CaMnO_3 . For binary and ternary sub-phases, a dense enough set of k -points was used so that the total energy is converged. The ionic relaxation parameters are chosen so that the forces in the surface and bulk structures are lower than 2 meV/Å.

We use density functional perturbation theory [24, 25] to calculate phonon frequencies and vibrational displacement vectors at the Γ point for all binary and ternary sub-phases in order to include the vibrational free energy contribution into the definition of the free energy. Translational symmetry is ensured by enforcing the three translational acoustic sum rules requiring that the acoustic modes have zero frequency. This is accomplished through small corrections to the diagonal elements of the dynamical matrix.

B. CaMnO_3 (001) Surface Structures

The (001) surface of CaMnO_3 is the lowest energy, since it consists of alternating CaO and MnO_2 planes, each of which is neutral in an ionic picture [26]. We construct surface structures with different compositions and reconstructions for both CaO and MnO_2 terminations, with symmetrical slabs of 7-9 layers and a vacuum gap between slabs of ≈ 15 Å. All atoms are fully relaxed.

Over 80 surface terminations are made by varying the stoichiometry of Ca, Mn and O

TABLE I. Energies per formula unit and magnetic moments on Mn atoms for bulk CaMnO_3 in different magnetic phases.

	FM	A-AFM	C-AFM	G-AFM
Energy (meV/formula unit)	38	12	4	0
Magnetic moment (μ_B/Mn)	2.75	2.68	2.64	2.61

including additional Ca_xO_y and Mn_xO_y layers in the $(\sqrt{2} \times \sqrt{2})R45^\circ$ surface symmetry. The positions of adatoms and additional layers are strategically selected; Ca and Mn atoms are placed on top of O atoms, and O species on top of Ca and Mn atoms. Each surface termination is identified based on its stoichiometric termination (either CaO or MnO_2) and whether its composition involves vacancies (-) or adatoms (+). As an illustration, $\text{CaO}+2.0\text{O}$ refers to a CaO-terminated surface with two oxygen adatoms per primitive unit cell of CaO. The number of adatoms and/or vacancies is tabulated per formula unit of either CaO or MnO_2 , even though there are two formula units in the surface super cell. Similarly, $\text{MnO}_2-0.5\text{Mn}-0.5\text{O}$ refers to a MnO_2 -terminated surface with one Mn vacancy and one oxygen vacancy per two MnO_2 units. Illustrations of the thermodynamically stable surface terminations after relaxation are shown in Fig. 1. These surface phases include (a,b) the stoichiometric surfaces, (c,d) their full surface coverage with adsorbed oxygen molecules, (e) the MnO_2 -terminated surface with one Mn vacancy and one oxygen vacancy, as well as (f) a CaO-terminated surface where a Mn adatom occupies a Ca vacancy. The last two surface phases (g,h) are stable at high temperatures but represent very exotic surface structures, as the ^aMn adatoms and ^aO adatoms have different coordination than the stoichiometric atoms, potentially indicating active sites.

The ferromagnetic (FM) and three AFM phases of bulk CaMnO_3 were analyzed. The A-AFM state has FM planes of alternating direction along the z -axis. The C-AFM arrangement consists of a Mn with nearest neighbors of opposite spin in the plane, and parallel spins between one plane and the next, while G-type AFM arranges the spins so that all nearest neighbors have opposite spin orientation. The magnetic ground state of bulk CaMnO_3 is found to be G-AFM $Pnma$ insulator, as reported in previous theoretical and experimental studies [21, 22, 27]. Our computed electronic band gap is 0.65 eV, significantly underestimating the experimental value of 3.1 eV [28] but in close agreement with previous computational

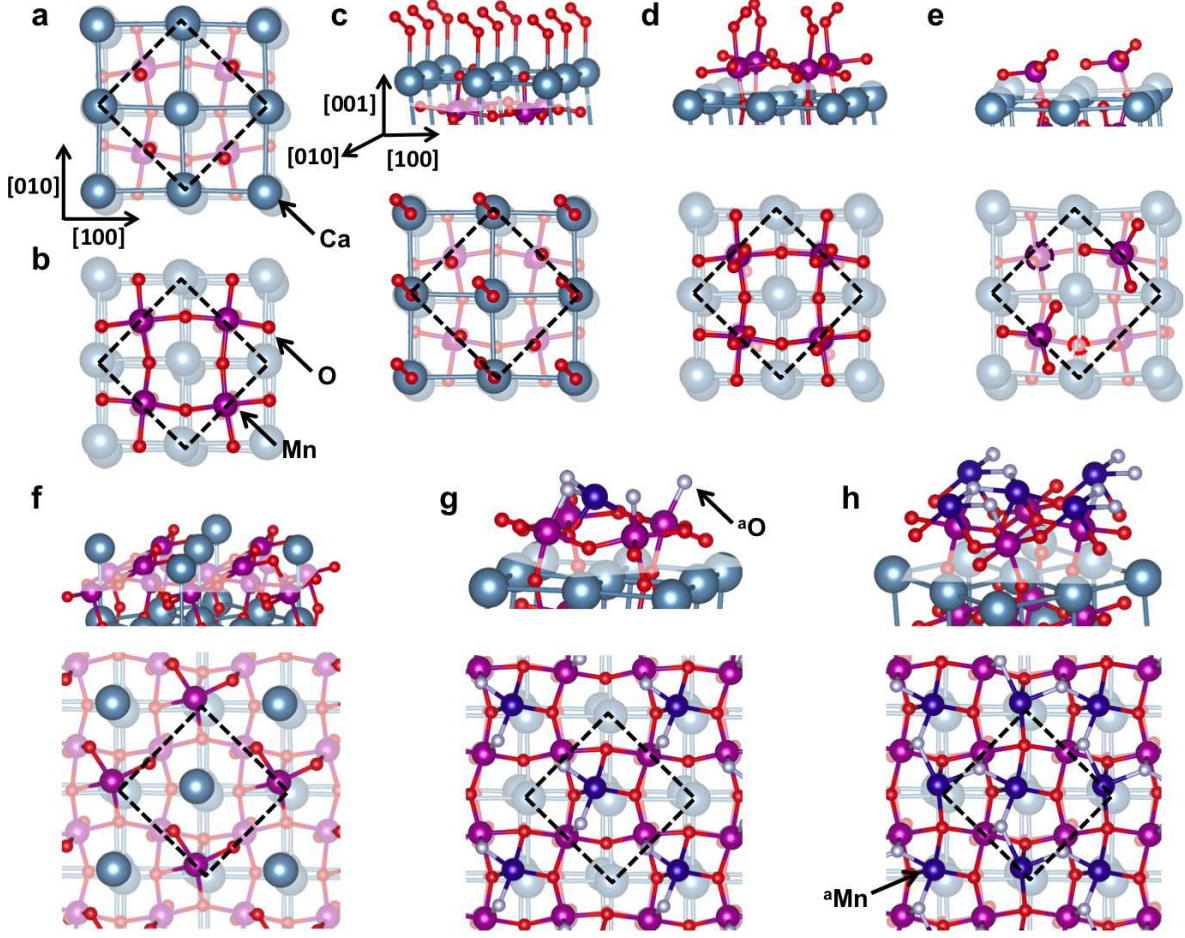


FIG. 1. Relaxed atomic structures of CaMnO_3 (001) thermodynamically stable surface reconstructions: Stoichiometric (a) CaO -terminated, (b) MnO_2 -terminated, (c) $\text{CaO}+2.0\text{O}$, (d) $\text{MnO}_2+2.0\text{O}$, (e) $\text{MnO}_2-0.5\text{Mn}-0.5\text{O}$, (f) $\text{CaO}-0.5\text{Ca}+0.5\text{Mn}$, (g) $\text{MnO}_2+0.5\text{Mn}+1.0\text{O}$, and (h) $\text{MnO}_2+1.0\text{Mn}+1.0\text{O}$. Large light blue spheres: Ca; medium purple spheres: Mn; and small red spheres: O. All surface reconstructions are within a $(\sqrt{2} \times \sqrt{2})R45^\circ$ surface periodicity, denoted with black dashed lines. Top and side views of the surface are shown for reconstructions on figures (c-h). For (e), the dashed purple and red circles represent the Mn vacancy and O vacancy, respectively. For (g,h), the ^aO and ^aMn atoms are O and Mn adatoms colored white and blue, respectively.

work [27, 29] The atom-projected magnetic moments of Mn atoms in each magnetic phase are shown in Table 2 as well as the relative energies with respect to the stable G-AFM phase, which are in very good agreement with those of a recent projector augmented wave calculation using the PBE functional [29]. The surface calculations are performed with G-AFM

ordering, magnetic spin flip at the surface and other possible magnetic spin configurations for surfaces with complex Mn_xO_y reconstructions (See Supplementary Material). The magnetic spin flip configuration is studied for all MnO_2 -based surfaces since stoichiometric MnO_2 is found to be more energetically favorable when all the surface spins flip (making the top and second layers FM aligned) [8].

C. Thermodynamic Stability

The free energies of CaMnO_3 (001) surfaces are calculated with the thermodynamic approach described in this section. In this model, the CaMnO_3 bulk is considered to be in contact with an atmosphere composed of all its components in equilibrium. This implies that the system acts as a reservoir where removal and/or addition of any of its components at the surface leads to a range of thermodynamically stable reconstructions and compositions at different conditions. The oxygen chemical potential, μ_{O} , is used to correlate the surface stability with environmental conditions such as temperature, T , and oxygen partial pressure, $p(\text{O}_2)$.

The surface free energy, Ω^i , of an individual surface slab, i , is defined as the excess amount of free energy needed to create the surface from its bulk form [11],

$$\begin{aligned}\Omega^i &= \frac{1}{2A} \left[G_{\text{slab}}^i - \sum_j N_j^i \mu_j \right] \\ &= \frac{1}{2A} \left[G_{\text{slab}}^i - N_{\text{Ca}}^i \mu_{\text{Ca}}^i - N_{\text{Mn}}^i \mu_{\text{Mn}}^i - N_{\text{O}}^i \mu_{\text{O}}^i \right].\end{aligned}\quad (1)$$

The Gibbs free energy of the slab is denoted by G_{slab}^i . The term $\sum_j N_j^i \mu_j$ represents the free energy of the material in slab i as the sum of the chemical potentials from the bulk of each component, μ_j , multiplied by the number of its atoms in each slab, N_j^i [30]. The factor of $\frac{1}{2}$ is included to account for top and bottom slabs. The surface free energy is reported as energy per unit area.

The $\Gamma_{m,n}^i$ term shown in Eq. (2) accounts for the off-stoichiometric atoms of component n with respect to component m in any surface slab i by relating the number of atoms of components N_m and N_n in the slab to their ratio in the bulk,

$$\Gamma_{m,n}^i = \frac{1}{2A} \left(N_n^i - N_m^i \frac{N_n^{\text{bulk}}}{N_m^{\text{bulk}}} \right). \quad (2)$$

In our case, the non-stoichiometric surface components were defined with respect to Mn atoms. Defining $\Gamma_{m,n}^i$ with respect to Ca atoms does not change the results. Next, Eqs. (1) and (2) are merged to express the Gibbs surface free energy as

$$\Omega^i = \frac{1}{2A} [G_{\text{slab}}^i - N_{\text{Mn}}^i(\mu_{\text{Ca}} + \mu_{\text{Mn}} + 3\mu_{\text{O}})] - \Gamma_{\text{Mn,Ca}}^i \mu_{\text{Ca}} - \Gamma_{\text{Mn,O}}^i \mu_{\text{O}}. \quad (3)$$

Since the system acts as a thermodynamic reservoir, the chemical potentials of CaMnO_3 components are not independent; they are related to the chemical potential of CaMnO_3 crystal, μ_{CaMnO_3} . The Gibbs free energy of bulk CaMnO_3 per formula unit, $g_{\text{CaMnO}_3}^{\text{bulk}}$, is then equal to μ_{CaMnO_3} because the slabs must be in equilibrium with the bulk as shown below:

$$\mu_{\text{Ca}} + \mu_{\text{Mn}} + 3\mu_{\text{O}} = \mu_{\text{CaMnO}_3} = g_{\text{CaMnO}_3}^{\text{bulk}}. \quad (4)$$

Inserting the relationship above into Eq. (3) simplifies the surface free energy to

$$\Omega^i = \frac{1}{2A} [G_{\text{slab}}^i - N_{\text{Mn}}^i g_{\text{CaMnO}_3}^{\text{bulk}}] - \Gamma_{\text{Mn,Ca}}^i \mu_{\text{Ca}} - \Gamma_{\text{Mn,O}}^i \mu_{\text{O}}. \quad (5)$$

The bulk stability region is defined by a set of boundary conditions [31–34]. First, Ca and Mn are not allowed to form metallic precipitates by satisfying the following conditions:

$$\mu_{\text{Ca}} \leq g_{\text{Ca}}^{\text{bulk}}, \quad (6)$$

$$\mu_{\text{Mn}} \leq g_{\text{Mn}}^{\text{bulk}}. \quad (7)$$

Second, the bulk is stable, while binary metal oxides derived from its components do not precipitate:

$$\mu_{\text{Ca}} + \mu_{\text{O}} \leq g_{\text{CaO}}^{\text{bulk}}, \quad (8)$$

$$\mu_{\text{Mn}} + \mu_{\text{O}} \leq g_{\text{MnO}}^{\text{bulk}}, \quad (9)$$

$$3\mu_{\text{Mn}} + 4\mu_{\text{O}} \leq g_{\text{Mn}_3\text{O}_4}^{\text{bulk}}, \quad (10)$$

$$2\mu_{\text{Mn}} + 3\mu_{\text{O}} \leq g_{\text{Mn}_2\text{O}_3}^{\text{bulk}}, \quad (11)$$

$$\mu_{\text{Mn}} + 2\mu_{\text{O}} \leq g_{\text{MnO}_2}^{\text{bulk}}. \quad (12)$$

Third, there should be no precipitation of other ternary sub-phases ($\text{Ca}_x\text{Mn}_y\text{O}_z$) from the bulk CaMnO_3 . The experimental phase diagram of bulk CaMnO_3 illustrates the importance of considering these ternary sub-phases, as they can co-exist with CaMnO_3 [35, 36].

Consequently, the following conditions must be met:

$$\mu_{\text{Ca}} + 2\mu_{\text{Mn}} + 4\mu_{\text{O}} \leq g_{\text{CaMn}_2\text{O}_4}^{\text{bulk}}, \quad (13)$$

$$\mu_{\text{Ca}} + 7\mu_{\text{Mn}} + 12\mu_{\text{O}} \leq g_{\text{CaMn}_7\text{O}_{12}}^{\text{bulk}}, \quad (14)$$

$$2\mu_{\text{Ca}} + \mu_{\text{Mn}} + 4\mu_{\text{O}} \leq g_{\text{Ca}_2\text{MnO}_4}^{\text{bulk}}, \quad (15)$$

$$3\mu_{\text{Ca}} + 2\mu_{\text{Mn}} + 7\mu_{\text{O}} \leq g_{\text{Ca}_3\text{Mn}_2\text{O}_7}^{\text{bulk}}, \quad (16)$$

$$4\mu_{\text{Ca}} + 3\mu_{\text{Mn}} + 10\mu_{\text{O}} \leq g_{\text{Ca}_4\text{Mn}_3\text{O}_{10}}^{\text{bulk}}. \quad (17)$$

The DFT energy is taken as the Helmholtz free energy at 0 K with zero-point energy, so the Gibbs free energy and the DFT energy are related as follows [11],

$$G = E^{\text{total}} + F^{\text{vib}} - TS^{\text{conf}} + pV \approx E + F^{\text{vib}}. \quad (18)$$

The energetic contributions provided by the pV and the configurational entropy TS^{conf} terms to the thermodynamic stability are considered to be negligible, as has been proven in previous studies [31–34].

The term F^{vib} , which is equal to $E^{\text{vib}} - TS^{\text{vib}}$, is calculated from the vibrational modes of the system. The phonon density of states, $\sigma(\omega)$, is used to express F^{vib} as an integral over frequency, ω :

$$F^{\text{vib.}} = \int d\omega F^{\text{vib.}}(T, \omega) \sigma(\omega). \quad (19)$$

The analytical expression of the harmonic quantum vibrational free energy per mode as a function of temperature and frequency, $F^{\text{vib}}(T, \omega)$, can be written as

$$F^{\text{vib.}}(T, \omega) = \frac{1}{2}\hbar\omega - k_B T \ln \left(1 - e^{-\frac{\hbar\omega}{k_B T}} \right). \quad (20)$$

Once the Gibbs free energy of each compound is calculated, the stability region of bulk CaMnO_3 as a function of T can be evaluated [31]. The vibrational free energy is included for all bulk phases while it is neglected for all slab structures [32–34]. The surface vibrational behavior is complex, and the vibrational modes could be affected by the electronic redistribution at the surface region; however, it has been shown for other systems that the phonon frequencies do not vary the order of stable surface phases [31].

The chemical potential for each component of CaMnO_3 is defined as its difference from

TABLE II. Experimental and computed formation energies (eV/formula unit) for binary and ternary sub-phases defining the bulk stability region of CaMnO_3 . The calculated formation energies for all Mn-based phases were performed with their corresponding magnetic ground-state structure, noted next to the compound. The experimental values are obtained from Ref. [40].

	Experimental	Theoretical
CaO	-6.59	-6.71
MnO (AFM-II ^a)	-3.99	-4.06
Mn ₃ O ₄ (FiM-III ^b)	-14.38	-15.46
Mn ₂ O ₃ (FM)	-9.93	-11.36
MnO ₂ (AFM)	-5.39	-6.60
CaMn ₂ O ₄ (AFM)	—	-18.23
CaMn ₇ O ₁₂ (NC-AFM)	—	-47.01
Ca ₂ MnO ₄ (G-AFM)	—	-20.56
Ca ₃ Mn ₂ O ₇ (G-AFM)	—	-34.34
Ca ₄ Mn ₃ O ₁₀ (G-AFM)	—	-48.12
CaMnO ₃ (G-AFM)	-12.83	-13.79

^a FM layers in the [111] plane and successive antiparallel layers.

^b Ferrimagnetic with Mn atoms ($\uparrow\uparrow\downarrow\downarrow\uparrow\uparrow$) in the corresponding order as Ref. [40].

the total energy of its reference state:

$$\Delta\mu_{\text{Ca}} = \mu_{\text{Ca}} - \left(E_{\text{Ca}}^{\text{bulk}} + F_{\text{Ca}}^{\text{vib,bulk}} \right), \quad (21)$$

$$\Delta\mu_{\text{Mn}} = \mu_{\text{Mn}} - \left(E_{\text{Mn}}^{\text{bulk}} + F_{\text{Mn}}^{\text{vib,bulk}} \right), \quad (22)$$

$$\Delta\mu_{\text{O}} = \mu_{\text{O}} - \frac{1}{2} \left(E_{\text{O}_2}^{\text{gas}} + F_{\text{O}_2}^{\text{vib,gas}} \right). \quad (23)$$

For the metals Ca and Mn, the reference energy is the DFT total energy and vibrational free energy of the elemental bulk crystal. For oxygen, the reference is the energy of an O atom in an isolated O₂ molecule. The $E_{\text{O}_2}^{\text{gas}}$ is corrected so that $E_{\text{O}_2}^{\text{gas}} = 2E_{\text{O}} + E_{\text{binding}}^{\text{expt}}$ [33] since a known shortcoming of DFT is the overestimation of binding energies [37], particularly for double bonds [38, 39].

Combining the chemical potential expressions, Eq. (21-23), and the approximation to the

Gibbs free energy for the slabs and CaMnO_3 bulk leads to the following expression for the Gibbs surface free energy,

$$\Omega^i = \frac{1}{2A} \left[E_{\text{slab}}^i - N_{\text{Mn}}^i \left(E_{\text{CaMnO}_3}^{\text{bulk}} + F_{\text{CaMnO}_3}^{\text{vib,bulk}} \right) \right] - \left[\Gamma_{\text{Mn,Ca}}^i \left(\Delta\mu_{\text{Ca}} + E_{\text{Ca}}^{\text{bulk}} + F_{\text{Ca}}^{\text{vib,bulk}} \right) + \Gamma_{\text{Mn,O}}^i \left(\Delta\mu_{\text{O}} + \frac{1}{2} \left(E_{\text{O}_2}^{\text{gas}} + F_{\text{O}_2}^{\text{vib,gas}} \right) \right) \right]. \quad (24)$$

The same approach including the vibrational free energy is applied to Eq. (4), whose expression is rewritten introducing the formation energy, $\Delta E_{\text{f}}^{\text{bulk}}$, as follows,

$$\Delta\mu_{\text{Ca}} + \Delta\mu_{\text{Mn}} + 3\Delta\mu_{\text{O}} = \Delta E_{\text{f,CaMnO}_3}^{\text{bulk}} + F_{\text{CaMnO}_3}^{\text{vib,bulk}}. \quad (25)$$

This equation is then used to rearrange all the bulk stability boundary inequalities, Eq. (6-17), so that only μ_{Ca} and μ_{O} are kept as variables. For instance, Eq. (15) becomes

$$\Delta\mu_{\text{Ca}} + \Delta\mu_{\text{O}} \leq \Delta E_{\text{f,Ca}_2\text{MnO}_4}^{\text{bulk}} - \Delta E_{\text{f,CaMnO}_3}^{\text{bulk}} + F_{\text{Ca}_2\text{MnO}_4}^{\text{vib,bulk}} - F_{\text{CaMnO}_3}^{\text{vib,bulk}}. \quad (26)$$

The results from the DFT formation energies, $\Delta E_{\text{f}}^{\text{bulk}}$, for all the binary and ternary sub-phases are compared to experimental quantities in Table 2. The formation energies are slightly overestimated, which is a well-known shortcoming of DFT [41].

The surface phase diagram dependence on T and $p(\text{O}_2)$ provides insightful physical interpretations of the experimental range of conditions for the surface stability. The $\Delta\mu_{\text{O}}$ can be directly related to T and $p(\text{O}_2)$ by the ideal gas approximation, since at equilibrium the μ_{O} in CaMnO_3 bulk is equal to the chemical potential of oxygen gas in the environment, $\mu_{\text{O}} = \frac{1}{2}\mu_{\text{O}_2}^{\text{gas}}(T, p)$. This leads to

$$\Delta\mu_{\text{O}}(T, p) = \Delta\mu_{\text{O}}(T, p^0) + \frac{1}{2}kT \ln \left(\frac{p}{p^0} \right) \quad (27)$$

where $\Delta\mu_{\text{O}}(T, p^0) = \frac{1}{2}\Delta G_{\text{O}_2}^{\text{gas}}(T, p^0)$. Thermodynamic data from the NIST-JANAF thermochemical tables [42] are used to determine the values of $\Delta\mu_{\text{O}}(T, p^0)$ by selecting the reference state for $\frac{1}{2}\Delta G_{\text{O}_2}^{\text{gas}}(T, p^0)$ extrapolated to $T=0$ K and $p(\text{O}_2)=1$ atm. Then, the values obtained are plotted for a temperature range of 0–3000 K at different $p(\text{O}_2)$ to correlate the stable surface phases with controlled environmental conditions.

III. RESULTS AND DISCUSSION

A. Magnetic Surface Reconstruction

Depending on their surface composition, some of the MnO_2 -based slabs undergo a magnetic spin flip reconstruction at the surface [8] that is energetically favorable, leading to lower total energy and greater surface stability. This magnetic spin flip reconstruction refers to a surface with G-AFM bulk order, but where the Mn spins in the surface layer align with the spins of the Mn in the second layer, generating a bilayer with C-type AFM alignment, as shown in Fig. 2(a,c). This occurs when the surface breaks the degeneracy of e_g and t_{2g} states, as the Mn cage is changed from octahedral to square pyramidal. This leads to the partial occupation of the e_g d_{z^2} bands at the surface, which favors the FM alignment of spins between the surface and subsurface MnO_2 layers.

In bulk CaMnO_3 , the superexchange magnetic interactions between the filled t_{2g} shells and the formally empty e_g shells determine the G-AFM ordering. However, this G-AFM ordering does not extend to the (001) MnO_2 -terminated surfaces, since double-exchange governs the magnetic interaction between Mn subsurface and surface. The Mn 3d orbital-projected density of states (DOS) of both G-AFM and spin flip surface and subsurface layers of the MnO_2 -terminated stoichiometric surface are shown in Fig. 2(b,d). The surface states of both G-AFM and spin-flip show the broken degeneracy of $e_g \rightarrow d_{x^2-y^2}$, d_{z^2} and $t_{2g} \rightarrow d_{xy}$, (d_{xz}, d_{yz}) , as expected for square pyramidal. The G-AFM subsurface states have degenerate e_g and t_{2g} shells; however, the spin-flip subsurface e_g degeneracy is broken, as the d_{z^2} is favorably aligned with the d_{z^2} from its neighboring surface state. The alignment of the Mn spins on surface and subsurface layers is induced by a double-exchange process, which is enabled by the occupation of the d_{z^2} orbital, lowering the energy of MnO_2 -terminated surfaces with the spin flip arrangement. Our DFT computed stoichiometric MnO_2 -surface yields a spin flip structure as its magnetic ground state, with an energy lowering relative to G-AFM of 15 meV per primitive surface cell.

Based on the prevalence of the energetically favorable magnetic spin flip reconstruction on the stoichiometric MnO_2 -terminated surface, it is important to study the effect of magnetic reconstruction on surface stability. All the MnO_2 -based surface reconstructions were relaxed with both G-AFM and spin flip magnetic ordering. Different magnetic configurations were

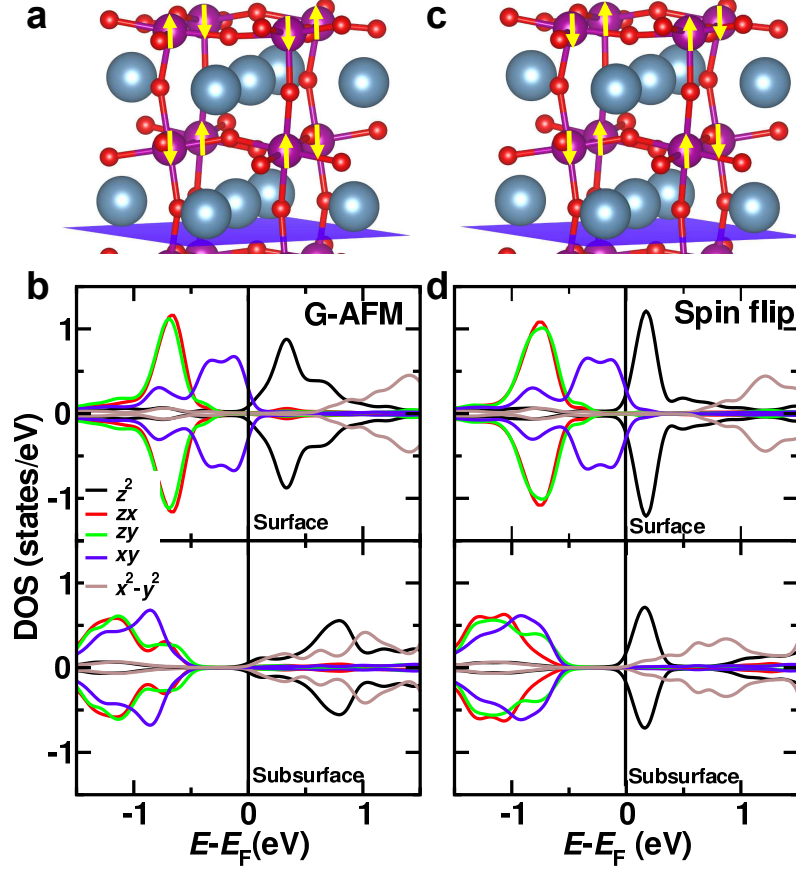


FIG. 2. Spin-flip magnetic reconstruction at the stoichiometric MnO_2 -terminated surface. The atomic, electronic and magnetic structure of the stoichiometric MnO_2 -terminated surface adopting (a,b) the bulk magnetic configuration, G-AFM, and (c,d) an energetically more favorable magnetic reconstruction where the spins of the surface Mn atoms are flipped. The magnetic spins are represented by the yellow arrows. The orbital-projected densities of states (DOS) for surface and subsurface Mn d -orbitals of the (b) G-AFM, and (d) spin-flip magnetic structures show different energetic alignment of the $3d_{z^2}$ orbital between surface and subsurface states.

explored for CaO-terminated surfaces with Mn adatoms as well as MnO_2 terminated surfaces with Mn_xO_y adatom reconstructions (See Supplementary Material). Half of the thermodynamically stable MnO_2 -based surfaces are magnetic spin flip configurations, as shown in Fig. 3 (surface phases with red grid lines). For surface reconstructions with only one extra Mn adatom, the spin arrangement that makes a local FM alignment between the surface Mn adatom and the nearest Mn atom is more favorable. For example, the local FM alignment between the Mn surface adatom and the Mn on the subsurface layer in CaO-0.5Ca+0.5Mn ,

which is within the bulk stability region, is 12 meV per primitive surface cell more stable than a local AFM alignment (See Supplementary Material).

B. Surface Phase Diagram

The computed surface phase diagram of CaMnO_3 , generated after calculating the surface free energy of the atomic and magnetic lowest energy configuration of each surface phase, is shown in Fig. 3. This diagram predicts a total of fourteen thermodynamically stable surface phases in the given range of $\Delta\mu_{\text{Ca}}$ and $\Delta\mu_{\text{O}}$. The phase diagram can be divided into four different quadrants based on conditions of $\Delta\mu_{\text{O}}$, $\Delta\mu_{\text{Ca}}$ and $\Delta\mu_{\text{Mn}}$. Even though $\Delta\mu_{\text{Mn}}$ is not directly plotted, its value can always be deduced from Eq. (25). The upper left quadrant (I) shows oxygen rich and cation poor conditions; therefore, the favored phases are terminations with excess oxygen adatoms, denoted as $\text{MnO}_2+2.0\text{O}$, $\text{CaO}+2.0\text{O}$ and $\text{CaO}+1.0\text{O}$. This quadrant also shows stability of the stoichiometric CaO - and MnO_2 -terminated surfaces as well as MnO_2 -based reconstructions, $\text{MnO}_2-0.5\text{Mn}-0.5\text{O}$ and $\text{MnO}_2+0.5\text{Mn}+1.0\text{O}$. In quadrant (II), both O and Ca are plentiful, leading to the absence of MnO_2 -terminated stable surfaces and the presence of Ca adatoms in stable CaO -based surfaces, $\text{CaO}+1.0\text{Ca}+2.0\text{O}$ and $\text{CaO}+1.0\text{Ca}+1.0\text{O}$. The bottom right quadrant (III) involves oxygen-poor but relatively Ca-rich conditions. This region is characterized by stable surfaces with MnO_2 termination, denoting that even though Ca is at high concentrations, MnO_2 -terminated surfaces are more favorable at oxygen poor conditions, clearly indicated by a surface phase where a Ca vacancy is filled by a Mn adatom, $\text{CaO}-0.5\text{Ca}+0.5\text{Mn}$. In the left bottom quadrant (IV), Mn is at its richest condition since both O and Ca are at poor levels. This promotes the large stable region for both $\text{MnO}_2+1.0\text{Mn}+1.0\text{O}$ and $\text{MnO}_2+2.0\text{Mn}+2.0\text{O}$.

A boundary line from the top left to mid-bottom right corners of the diagram delimits the regions of CaO - (upper) and MnO_2 - (lower) terminated surfaces. Six different CaO -terminated surfaces are found, many of them covering a significant area of chemical potential space. On the other hand, MnO_2 -type phases generally show smaller stable regions with a higher variety of phases, which can be explained by the multivalency of Mn. For instance, the predicted path from $\text{MnO}_2+2.0\text{Mn}+2.0\text{O}$ to $\text{MnO}_2+2.0\text{O}$ consists of a complex series of transitions. These transitions occur by increasing the $\Delta\mu_{\text{O}}$ from -3.0 eV to -0.5 eV while keeping constant the $\Delta\mu_{\text{Ca}}$ at ≈ -7.0 eV. The changes in $\Delta\mu_{\text{O}}$ can be controlled experimen-

tally by varying T or $p(\text{O}_2)$. For example, these surface phase transitions are predicted to occur at a constant $p(\text{O}_2)$ of 10^{-10} atm, as the temperature is decreased from ≈ 1400 K to ≈ 400 K. Starting with the surface initially at ≈ 1400 K in the $\text{MnO}_2+2.0\text{Mn}+2.0\text{O}$ phase, as the temperature is reduced to ≈ 750 K, the desorption of oxygen atoms is thermodynamically favorable, leading to the surface reconstruction $\text{MnO}_2+1.0\text{Mn}+1.0\text{O}$. Reducing the temperature further to ≈ 600 K should cause the surface to reconstruct into $\text{MnO}_2+0.5\text{Mn}+1.0\text{O}$ and even co-exist with stoichiometric MnO_2 -terminated surface. Once the temperature reaches ≈ 400 K, the surface phase transition to $\text{MnO}_2+2.0\text{O}$ is thermodynamically favored.

The slopes of the boundaries between phases directly relate to the changes in numbers of surface atoms of each species. The $\text{CaO}+2.0\text{O}$ surface phase changes to $\text{CaO}+1.0\text{Ca}+2.0\text{O}$ at a vertical boundary of $\Delta\mu_{\text{Ca}} \approx -5.75$ eV via adsorption of Ca cations. Similarly, horizontal lines at $\Delta\mu_{\text{O}} \approx -0.8$ eV and ≈ -0.9 eV denotes its transition to $\text{CaO}+1.0\text{O}$ and stoichiometric CaO , respectively, by the removal of oxygen adatoms. Between these extremes, the slope of the CaO to $\text{CaO}+1.0\text{Ca}+2.0\text{O}$ transition, as indicated in Fig. 3, is $-\frac{1}{2}$, suggesting the addition of 2 Ca cations and 4 oxygen atoms per cell since the transition line will be crossed by moving toward Ca- and O-rich conditions. Taking into account the relationship shown in Eq. (25), the slope of the boundaries between surface phases can then be defined as $\frac{(a-b)}{(3b-c)}$, where a , b , and c represent the net change in number of Ca, Mn, and O atoms, respectively, between phases. For example, the removal of 2 Mn atoms and the adsorption of 2 oxygen atoms per cell results in the transition of surface phase $\text{MnO}_2+2.0\text{Mn}+2.0\text{O}$ to $\text{MnO}_2+1.0\text{Mn}+1.0\text{O}$. This is in agreement with the boundary for this phase transition having slope of $-\frac{1}{4}$.

Stability Region

The surface phase diagram shows a series of stable surfaces, but only a few of them are within the bulk stability region. The ternary sub-phases illustrated in Eqs. 13-17 are included in the definition of the stability region since an extensive experimental examination of the phase relations of Ca-Mn-O bulk systems [35, 36] found the co-existence lines for the CaMnO_3 phase with these ternary sub-phases, and correspondingly narrower stability boundaries for CaMnO_3 . The boundary of bulk phase stability is defined by Ca_2MnO_4 , $\text{Ca}_3\text{Mn}_2\text{O}_7$, and $\text{Ca}_4\text{Mn}_3\text{O}_{10}$ on the top and Mn_2O_3 , MnO_2 , CaMn_2O_4 , and $\text{CaMn}_7\text{O}_{12}$ on

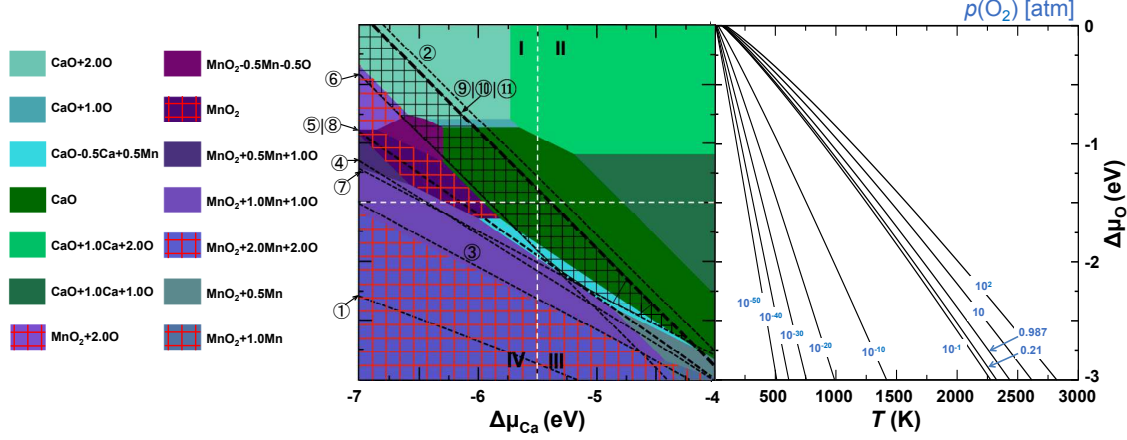


FIG. 3. Surface phase diagram of CaMnO_3 with Mn metallic, binary, and ternary sub-phase bulk stability boundaries at $T=0$ K denoted as follows (1)Mn, (2)CaO, (3)MnO, (4) Mn_3O_4 , (5) Mn_2O_3 , (6) MnO_2 , (7) CaMn_2O_4 , (8) $\text{CaMn}_7\text{O}_{12}$, (9) Ca_2MnO_4 , (10) $\text{Ca}_3\text{Mn}_2\text{O}_7$, and (11) $\text{Ca}_4\text{Mn}_3\text{O}_{10}$. The enclosed area shaded by black grid lines represents the bulk stability region. The phase diagram is divided into four regions, with dashed white lines to group phases with thermodynamic stability at similar condition ranges of $\Delta\mu_{\text{O}}$, $\Delta\mu_{\text{Ca}}$, and $\Delta\mu_{\text{Mn}}$. The color-coded legend for each of the surface phases is on the left panel. The phases with red grid lines represent surfaces with spin-flip magnetic reconstructions. The right panel shows the T and $p(\text{O}_2)$ dependence of $\Delta\mu_{\text{O}}$.

the bottom (lines 9-11 and 5-8, respectively, shown in Fig. 3).

A confirmation of the importance of including the ternary sub-phases is the ability of this model to describe the decomposition of bulk CaMnO_3 . Experimentally, decomposition of CaMnO_3 occurs at ≈ 1700 K and 0.21 atm O_2 [35]. Using the DFT-generated stability region computed at 0 K, this decomposition temperature is predicted to be ≈ 2100 K at 0.21 atm by considering the decomposition conditions at the low $\Delta\mu_{\text{O}}$ end of the bulk stability region. However, if boundaries 7-11 are neglected, then the stability region is limited by MnO_2 , Mn_2O_3 and Mn_3O_4 on the bottom and bordered by CaO on the top (lines 6, 5, 4, and 2, respectively, in Fig. 2), artificially increasing the computed decomposition temperature to over 2500 K at 0.21 atm.

These ternary sub-phases include the Ruddlesden-Popper phases $\text{CaO}(\text{CaMnO}_3)_n$, which are perovskite structures with double CaO layer (001) planes with n layers of CaMnO_3 in between [43]. Naturally, the surface reconstruction with CaO double layer, $\text{CaO}+1.0\text{Ca}+1.0\text{O}$, is found on the side where the Ruddlesden-Popper phases $\text{CaO}(\text{CaMnO}_3)_n$ limit the stabil-

ity of the CaMnO_3 bulk. The CaMn_2O_4 phase is a marokite structure [44], where the MnO_6 octahedra share edges and corners. This network of octahedra leads to channels along the a -axis which provide Ca atoms with 8-coordinated sites. It has been found that this marokite-type phase shows potential photocatalytic activity [45]. This bulk phase borders the surface phase with a MnO_2 -terminated layer that has an additional MnO layer, $\text{MnO}_2+1.0\text{Mn}+1.0\text{O}$. $\text{CaMn}_7\text{O}_{12}$ is a complex distorted double perovskite, whose chemical formula is formally written as $(\text{CaMn}_3^{+3})(\text{Mn}_3^{+3}\text{Mn}^{+4})\text{O}_{12}$. This perovskite-derived phase consists of $\frac{1}{4}$ of the A -sites occupied by Ca and the rest by Mn^{+3} , while the B -site charges are arranged via charge ordering below 440 K [46]. All these ternary sub-phases are stable for some range of chemical potentials [35, 36], defining realistic stability boundaries for the surface of CaMnO_3 .

Temperature Dependence

The bulk stability region described above is based on DFT calculations at 0 K enclosing the $\text{CaO}+2.0\text{O}$, $\text{CaO}+1.0\text{O}$, CaO , $\text{CaO}-0.5\text{Ca}+0.5\text{Mn}$, $\text{MnO}_2+2.0\text{O}$, and $\text{MnO}_2-0.5\text{Mn}-0.5\text{O}$ phases. A more accurate description of the stability region requires the inclusion of the vibrational free energy. This is significant, since it determines how the stability region changes as a function of temperature.

The bulk stability region is recalculated incorporating the bulk vibrational free energy at 573 K, 873 K and 1173 K, shown in Fig. 4. These temperatures are selected since they are within the range of experimental temperature conditions used in the synthesis and pulsed laser deposition of the CaMnO_3 crystal [47] and film, as well as in the annealing process for surface characterization techniques. These temperatures shift the stability region such that only MnO_2 -based surfaces are favored. As temperature increases, the stability region shifts towards Ca-poor and O-poor conditions, in agreement with previous studies on other surfaces [31, 33]. As the stability region moves, it encloses other phases that are predicted to be stable at those temperatures. At 573 K, the surface phases within the bulk stability region are the same as in Fig. 3, with the addition of the stoichiometric MnO_2 -terminated surface. Increasing the temperature by 300 K leads to the stability of $\text{MnO}_2+1.0\text{Mn}+1.0\text{O}$ surface phase. At 1173 K, the phases within the bulk stability region include the $\text{MnO}_2+0.5\text{Mn}+1.0\text{O}$ phase. The clear trend is that the surface structures with

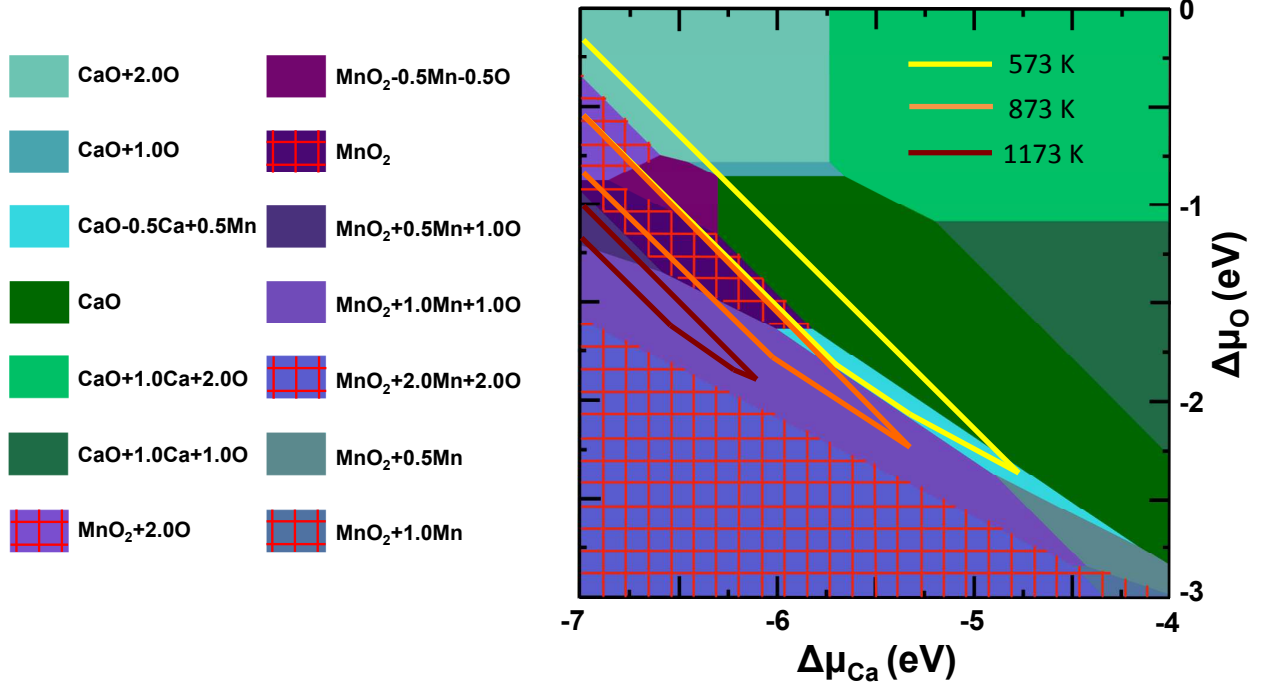


FIG. 4. Temperature dependence of the bulk stability region within CaMnO_3 surface phase diagram. Stability limits at different temperatures 573 K (yellow), 873 K (orange) and 1173 K (dark red) are plotted, indicating the thermodynamic stability of MnO_2 -terminated surface reconstructions.

MnO_2 terminations are more favorable at higher temperatures.

Changes in the shape of the stability region reflect how binary and ternary sub-phase boundaries shift as the vibrational free energy at various temperatures is included. Overall, the bulk stability region tends to shrink as the higher temperature contributions are included. This is in good agreement with previous reports, since it is experimentally observed that CaMnO_3 crystal decomposes at temperatures higher than ≈ 1700 K [35] and our theoretical bulk stability region vanishes around the same temperature.

IV. SUMMARY AND CONCLUSIONS

The energies of series of CaO - and MnO_2 -terminated CaMnO_3 (001) surfaces with different combinations of vacancies, adatoms and additional layers are reported using *ab initio* thermodynamics to theoretically predict the surface phase diagram. The predicted surface phase diagram has surface structures for both terminations, with stability ranges specified

by $\Delta\mu_{\text{O}}$ and $\Delta\mu_{\text{Ca}}$. The $\Delta\mu_{\text{O}}$ is related to T and $p(\text{O}_2)$, linking surface stability with experimental conditions.

The chemical potential region for which CaMnO_3 is the only bulk phase is bounded by coexistence lines with the Ruddlesden-Popper phases $\text{CaO}(\text{CaMnO}_3)_n$ (where $n=1, 2$, and 3), as well as Mn_2O_3 , MnO_2 , CaMn_2O_4 , and $\text{CaMn}_7\text{O}_{12}$. This shows the relevance of incorporating the ternary subphases from the experimental Ca-Mn-O compositional phase diagram [35, 36]. The surface phases that are favored within this bulk stability region change once the vibrational free energy at different temperatures is included. The stability region shifts to lower $\Delta\mu_{\text{Ca}}$ for higher T , leading to the predominance of complex MnO_2 -based surfaces at T above 800 K. Thermodynamically stable phases include potentially reactive surfaces, $\text{MnO}_2+1.0\text{Mn}+1.0\text{O}$, since it shows two unique Mn sites based on coordination.

The MnO_2 -based surfaces show intriguing atomic and magnetic structures which are comprehensively explored by computing the magnetic ground state and analyzing its thermodynamic stability. Some of the MnO_2 -terminated surfaces are energetically more favorable when their surface and subsurface spins are aligned. This occurs when the filling of the d_{z^2} orbital causes a more favorable double-exchange interaction between the subsurface and surface Mn atoms. The atomic composition of the surface affects this magnetic reconstruction; for some Mn_xO_y reconstructions, the surface reconstructs, rearranging the magnetic interactions in the system. However, this magnetic spin flip reconstruction prevails for key stable surfaces such as stoichiometric MnO_2 -terminated and $\text{MnO}_2+2.0\text{O}$.

This study addresses structures with $(\sqrt{2}\times\sqrt{2})R45^\circ$ surface symmetry, leading to ordered surfaces due to periodic boundary conditions. Admittedly, real surfaces are more complex and disordered; however, by taking into account the chemical and thermal contributions to the surface stability and exploring a wide range of possible surface structures, the predicted phase diagram provides an acceptable foundation for the analysis of experimental data on this surface. Consequently, this predicted surface phase diagram could lead to experimental studies performing low-energy electron diffraction and scanning tunneling microscopy to validate the stable surface reconstructions and further explore the surface evolution.

ACKNOWLEDGMENTS

D.S.-G. was supported by the Office of Naval Research under Grant No. N00014-11-1-0664. C.-W.L. was supported by the US Department of Energy Office of Basic Energy Sciences under Grant No. DE-FG02-07ER15920. D.Y. was supported by the National Science Foundation under Grant No. DMR-1124696. A.M.R. was supported by the National Science Foundation under Grant No. CMMI-1334241. Computational support was provided by the High-Performance Computing Modernization Office of the US Department of Defense, and the National Energy Research Scientific Computing Center of the US Department of Energy.

-
- [1] S. Bhattacharjee, E. Bousquet, and P. Ghosez, Phys. Rev. Lett. **102**, 117602 (2009).
 - [2] H. Wang, L. He, and X. Wu, EPL (Europhysics Letters) **100**, 17005 (2012).
 - [3] S. Urata, R. Funahashi¹, T. Mihara, A. Kosuga, S. Sodeoka, and T. Tanaka, International Journal of Applied Ceramic Technology **4**, 535 (2007).
 - [4] K. Koumoto, Y. Wang, R. Zhang, A. Kosuga, and R. Funahashi, Annual Review of Materials Research **40**, 363 (2010).
 - [5] Z. Zeng, M. Greenblatt, and M. Croft, Phys. Rev. B **59**, 8784 (1999).
 - [6] A. Kawashima, K. Matsubara, and K. Honda, Bioresource Technology **99**, 3439 (2008).
 - [7] M. M. Najafpour, B. Pashaei, and S. Nayeri, Dalton Trans. **41**, 4799 (2012).
 - [8] A. Filippetti and W. E. Pickett, Phys. Rev. Lett. **83**, 4184 (1999).
 - [9] A. Filippetti and W. E. Pickett, Phys. Rev. B **62**, 11571 (2000).
 - [10] T. T. Nguyen, T. C. Bach, H. T. Pham, T. T. Pham, D. T. Nguyen, and N. N. Hoang, Physica B: Condensed Matter **406**, 3613 (2011).
 - [11] K. Reuter and M. Scheffler, Phys. Rev. B **65**, 035406 (2001).
 - [12] J. P. Perdew, A. Ruzsinszky, G. I. Csonka, O. A. Vydrov, G. E. Scuseria, L. A. Constantin, X. Zhou, and K. Burke, Phys. Rev. Lett. **100**, 136406 (2008).
 - [13] P. Giannozzi, S. Baroni, N. Bonini, M. Calandra, R. Car, C. Cavazzoni, D. Ceresoli, G. L. Chiarotti, M. Cococcioni, I. Dabo, A. D. Corso, S. de Gironcoli, S. Fabris, G. Fratesi, R. Gebauer, U. Gerstmann, C. Gougoussis, A. Kokalj, M. Lazzeri, L. Martin-Samos,

- N. Marzari, F. Mauri, R. Mazzarello, S. Paolini, A. Pasquarello, L. Paulatto, C. Sbraccia, S. Scandolo, G. Sclauszero, A. P. Seitsonen, A. Smogunov, P. Umari, and R. M. Wentzcovitch, *J. Phys.:Condens. Matter* **21**, 395502 (2009).
- [14] W. Luo, A. Franceschetti, M. Varela, J. Tao, S. J. Pennycook, and S. T. Pantelides, *Phys. Rev. Lett.* **99**, 036402 (2007).
- [15] M. Cococcioni and S. de Gironcoli, *Phys. Rev. B* **71**, 035105 (2005).
- [16] A. M. Rappe, K. M. Rabe, E. Kaxiras, and J. D. Joannopoulos, *Phys. Rev. B Rapid Comm.* **41**, 1227 (1990).
- [17] N. J. Ramer and A. M. Rappe, *Phys. Rev. B* **59**, 12471 (1999).
- [18] <http://opium.sourceforge.net>.
- [19] M. Fuchs and M. Scheffler, *Comput. Phys. Commun.* **119**, 67 (1999).
- [20] D. Porezag, M. R. Pederson, and A. Y. Liu, *Phys. Rev. B* **60**, 14132 (1999).
- [21] K. R. Poeppelmeier, M. E. Leonowicz, J. C. Scanlon, J. M. Longo, and W. B. Longo, *J. Solid State Chem.* **45**, 71 (1982).
- [22] S. Bhattacharjee, E. Bousquet, and P. Ghosez, *J. Phys.: Condens. Matter* **20**, 255229 (2008).
- [23] H. J. Monkhorst and J. D. Pack, *Phys. Rev. B* **13**, 5188 (1976).
- [24] S. Baroni, S. de Gironcoli, and A. Dal Corso, *Rev. Mod. Phys.* **73**, 515 (2001).
- [25] X. Gonze, *Phys. Rev. A* **52**, 1096 (1995).
- [26] P. W. Tasker, *Journal of Physics C: Solid State Physics* **12**, 4977 (1979).
- [27] W. E. Pickett and D. J. Singh, *Phys. Rev. B* **53**, 1146 (1996).
- [28] J. H. Jung, K. H. Kim, D. J. Eom, T. W. Noh, E. J. Choi, J. Yu, Y. S. Kwon, and Y. Chung, *Phys. Rev. B* **55**, 15489 (1997).
- [29] H. Tsukahara, S. Ishibashi, and K. Terakura, *Phys. Rev. B* **81**, 214108 (2010).
- [30] J. W. Cahn, *Interfacial Segregation* (ASM, Metals, Park, OH, 1973) p. 3.
- [31] C.-W. Lee, R. K. Behera, E. D. Wachsman, S. R. Phillpot, and S. B. Sinnott, *Phys. Rev. B* **83**, 115418 (2011).
- [32] E. Heifets, E. A. Kotomin, Y. A. Mastrikov, S. Piskunov, and J. Maier, *Thermodynamics - Interaction studies - Solids, liquids and gases* (InTech Open Access Publishers, 2011) pp. 491–518.
- [33] A. M. Kolpak, D. Li, R. Shao, A. M. Rappe, and D. A. Bonnell, *Phys. Rev. Lett.* **101**, 036102 (2008).

- [34] S. V. Levchenko and A. M. Rappe, Phys. Rev. Lett. **100**, 256101 (2008).
- [35] H. S. Horowitz and J. M. Longo, Materials Research Bulletin **13**, 1359 (1978).
- [36] V. F. Balakirev and Y. V. Golikov, Inorganic Materials **42**, S49 (2006).
- [37] F. Furche, Phys. Rev. B **64**, 195120 (2001).
- [38] E. J. Walter and A. M. Rappe, Surf. Sci. **427**, 11 (1999).
- [39] I. Grinberg, Y. Yourdshahyan, and A. M. Rappe, J. Chem. Phys. **117**, 2264 (2002).
- [40] S. Fritsch and A. Navrotsky, Journal of the American Ceramic Society **79**, 1761 (1996).
- [41] E. A. Kotomin, Y. A. Mastrikov, E. Heifets, and J. Maier, Phys. Chem. Chem. Phys. **10**, 4644 (2008).
- [42] M. W. Chase Jr., J. Phys. Chem. Ref. Data, Monograph 9 , 1 (1998).
- [43] I. D. Fawcett, J. E. Sunstrom IV, M. Greenblatt, M. Croft, and K. V. Ramanujachary, Chemistry of Materials **10**, 3643 (1998).
- [44] C. D. Ling, J. Neumeier, and D. N. Argyriou, Journal of Solid State Chemistry **160**, 167 (2001).
- [45] W. Xue-Wei, Z. Hai-Xin, L. Xiao-Jun, and Z. Xing-Gan, Chinese Physics Letters **28**, 107101 (2011).
- [46] B. Bochu, J. Buevoz, J. Chenavas, A. Collomb, J. Joubert, and M. Marezio, Solid State Communications **36**, 133 (1980).
- [47] M. E. Melo Jorge, A. Correia dos Santos, and M. R. Nunes, International Journal of Inorganic Materials **3**, 915 (2001).